Changing black carbon transport to the Arctic from present day to the end of 21st century

Chaoyi Jiao and Mark G. Flanner

Department of Climate and Space Sciences and Engineering, University of Michigan

Keypoints:

(1) We explore changing Arctic aerosol transport and deposition in a warming climate

(2) Circulation changes enhance/reduce Arctic transport of East Asia/North America emissions

(3) More efficient wet removal substantially reduces Arctic BC lifetime and burden

C. Jiao and M. G. Flanner, Department of Climate and Space Sciences and Engineering, University of Michigan, Ann Arbor, MI, 48109. (chaoyij@umich.edu)

This is the author manuscript accepted for publication and has undergone full peer review but has not been through the copyediting, typesetting, pagination and proofreading process, which may lead to differences between this version and the Version of Record. Please cite this article as doi: 10.1002/2015JD023964

Abstract. Here, we explore how climate warming under the Representative Concentration Pathway 8.5 (RCP8.5) impacts Arctic aerosol distributions via changes in atmospheric transport and removal processes. We modify the bulk aerosol module in the Community Atmosphere Model to track distributions and fluxes of 200 black carbon-like tracers emitted from different locations, and we conduct idealized experiments with and without active aerosol deposition. Changing wind patterns, studied in isolation, cause the Arctic burdens of tracers emitted from East Asia and West Europe during winter to increase about 20% by the end of the century, while decreasing the Arctic burdens of North American emissions by about 30%. These changes are caused by an altered winter polar dome structure that results from Arctic amplification and inhomogeneous sea-ice loss and surface warming, both of which are enhanced in the Chukchi Sea region. The resulting geostrophic wind favors Arctic transport of East Asian emissions while inhibiting poleward transport of North American emissions. When active deposition is also considered, however, Arctic burdens of emissions from northern mid-latitudes show near-universal decline. This is a consequence of increased precipitation and wet removal, particularly within the Arctic, leading to decreased Arctic residence time. Simulations with present-day emissions of black carbon indicate a 13.6% reduction in the Arctic annual-mean burden by the end of the 21st century, due to warming-induced transport and deposition changes, while simulations with changing climate and emissions under RCP8.5 show a 61.0% reduction.

1. Introduction

Arctic climate has changed rapidly during recent decades, including increased surface temperature, reduced sea ice and land snow, and altered atmospheric circulation. One contributor to this change is altered distributions of absorptive aerosols (black carbon, brown carbon and dust) which are transported to the polar region, heat the atmosphere, and darken snow and ice surfaces [e.g., *Flanner et al.*, 2007; *Ramanathan and Carmichael*, 2008; *Bond et al.*, 2013]. The Arctic aerosol distribution is governed by three factors: emission, transport and deposition. The emission source within the Arctic is small [e.g., *Lamarque et al.*, 2010; *Browse et al.*, 2013] and hence emissions outside the Arctic contribute the majority of the Arctic aerosol burden via atmospheric transport [e.g., *Koch and Hansen*, 2005; *Law and Stohl*, 2007]. Understanding the transport and deposition processes that govern Arctic aerosols will help us to better constrain the Arctic aerosol budget. Furthermore, both the transport and deposition processes are subject to change associated with global climate warming. Thus it is our interest to examine those changes and investigate their influences on the Arctic aerosol budget.

The characteristics of aerosol transport and deposition have been examined in several studies. *Stohl* [2006] used a Lagrangian particle dispersion model to show that aerosol tracers emitted from North America and Asia generally experience uplift outside the Arctic and then can be transported into the Arctic. Pollution from Europe can travel to the Arctic by both low and high altitude pathways. *Shindell et al.* [2008] used a multi-model approach to reveal that European emissions dominate the surface aerosol and carbon monoxide budget of the Arctic, while emissions from East Asia are important for high altitude burden. They also concluded that Europe and North America are the two most dominant contributors to black carbon (BC) on Greenland,

with each contributing about 40% of the total BC deposition in that region. Along with aerosol transport to the Arctic, the removal processes that occur during the transport to and within the Arctic are equally important for the Arctic aerosol budget. *Garrett et al.* [2010] and *Garrett et al.* [2011] applied observations to show that the seasonality of both light absorbing and light scattering aerosols in the Arctic are controlled by wet scavenging. They argued that high relative humidity and warm temperatures would lead to more efficient removal of aerosols in spring and summer seasons. *Garrett et al.* [2011] also suggested that the Arctic might be cleaner in the future due to the projected warmer and wetter climate. *Liu et al.* [2011] found that simulated Arctic BC concentrations improved significantly compared to observations after adjusting the aerosol aging, dry deposition and wet removal processes represented in the GFDL AM3 model. *Zhou et al.* [2012] found that both the meteorological fields and the wet deposition treatment in their model have strong influences on BC concentrations and deposition in polar regions. *Wang et al.* [2013] evaluated and improved the aerosol processes, including aerosol–cloud interactions, cloud microphysics and macrophysics, aerosol transformation, convective transport and aerosol wet removal, in the Community Atmosphere Model version 5 (CAM5). They significantly improved the BC and sulfate distribution in the Arctic compared to observations, and identified wet removal, aerosol aging time and aerosol–cloud interactions as the most important processes that influence the remote aerosol budget.

Previous studies have explored features of global aerosol transport using Eulerian models with different tracer identification methods [e.g., *Koch and Hansen*, 2005; *Shindell et al.*, 2008; *Wang et al.*, 2011; *Ma et al.*, 2013; *Wang et al.*, 2014]. All of those studies either used explicit regional emission tags or emission sensitivity (perturbation) techniques to track and archive the temporal and spatial characteristics of aerosols emitted from different regions. Studies with

Lagrangian particle dispersion models can track the behavior of many individual tracers, which makes them ideal for studies of aerosol transport process [*Stohl*, 2006]. These models typically do not have sophisticated representations of aerosol removal processes, however, and it is our interest here to examine the relative impacts of changing aerosol transport and deposition in the context of Arctic climate change.

In this study, we combine merits of both modeling approaches. We modified the bulk aerosol module (BAM, [*Rasch et al.*, 2000]) component of CAM to explicitly simulate hundreds of tagged BC aerosol tracers. Each of these tagged tracers has a distinct emission source region. With the modeling framework developed for this study, we investigate how the aerosol tracer distribution from different emission locations is influenced solely by changes in atmospheric transport, and secondly by transport and deposition processes combined. Detailed description of the experiment design is in Section 2.

One of the primary objectives of this study is to investigate how warming of the climate system could affect the spatial distribution of aerosols emitted from different locations, especially in high latitude regions. This is motivated by numerous recent studies showing that there will be pronounced changes in Arctic circulation and climate associated with global climate warming [e.g., *Serreze et al.*, 2009; *Screen and Simmonds*, 2010; *Francis and Vavrus*, 2012; *Screen et al.*, 2012; *Bintanja and van der Linden*, 2013]. For example, *Serreze et al.* [2009] showed that surface and lower tropospheric Arctic air temperatures are projected to rise at a significantly faster pace than other regions of the northern hemisphere, in response to increasing greenhouse gas concentrations, especially during the winter season. This phenomenon is referred to as Arctic Amplification [*Holland and Bitz*, 2003; *Screen and Simmonds*, 2010]. *Francis and Vavrus* [2012] argued that Arctic Amplification could produce important changes in mid-latitude circu-

lation, including a weakening of zonal winds and an increase in Rossby wave amplitude, particularly during the fall and winter seasons. *Lee et al.* [2015] stated that anomalously warm sea surface temperatures and low sea ice concentrations in the Arctic led to recent mid-latitude winter atmospheric circulation anomalies. It follows that aerosol transport pathways to the Arctic will also change in concert with changing circulation patterns associated with Arctic amplification. Here, we run experiments with present day climate conditions as well as climate conditions and emissions at the end of the 21st century as simulated under the Representative Concentration Pathway 8.5 (RCP8.5) scenario. By comparing the simulations from those two climate states, we quantitatively analyze changes in aerosol transport pathways, column burdens, deposition fluxes and atmospheric lifetimes associated with emissions from different locations. In order to distinguish the characteristics of tracers emitted from different geographical locations, we resolve the major emission source regions in northern hemisphere mid-latitude regions with 200 tagged tracers. The number of different tagged tracers studied here is much larger than in other studies employing Eulerian transport models, but the relatively simple aerosol treatment of BAM permits such simulations to be conducted with modest computational expense.

2. Experiment Design

We use the coupled Community Atmosphere Model version 4 (CAM4), Community Land Model version 4 (CLM4), Community Ice Code (CICE) and Data Ocean Model within the framework of the Community Earth System Model version 1.1.1 (CESM1). The models are driven with prescribed annually-repeating sea surface temperature (SST) and sea ice fields. This model framework generally shows low biases in the simulated climatological fields such as surface temperature, sea ice fraction and precipitation, and has realistic representation of the El Niño – Southern Oscillation and Madden – Julian oscillation [*Gent et al.*, 2011]. Meanwhile,

Gent et al. [2011] also pointed out the CAM4 has relatively poor representation of the precipitation field in the tropical Pacific Ocean and the low cloud content in the Arctic. Previous studies have also evaluated the simulated aerosol fields of CAM4 with BAM [e.g., *Lamarque et al.*, 2011, 2012]. *Lamarque et al.* [2012] found that CAM4 tends to underestimate the aerosol optical depth over most regions compared to MODIS (Moderate Resolution Imaging Spectroradiometer) and MISR (Multi-angle Imaging SpectroRadiometer) satellite observations. In CAM4, the simulated sulfate fields generally agree with observations [*Lamarque et al.*, 2012]. Yet elemental carbon and organic carbon aerosol fields simulated by CAM4 show relatively large biases compared to near-surface measurements at the IMPROVE (United States Interagency Monitoring of Protected Visual Environments) sites [*Lamarque et al.*, 2012]. Some of the biases in CAM4, such as the underestimation of BC both near surface and in middle – high troposphere in Arctic, are also consistent with other models [e.g., *Koch et al.*, 2009; *Lee et al.*, 2013; *Eckhardt et al.*, 2015].

In this study, we run CAM4 at $2.5^\circ \times 1.9^\circ$ horizontal resolution with 26 hybrid sigma pressure layers. In order to record multiple tagged tracers in the model, we modify BAM to enable any number of BC-like aerosol tracers to be simulated. All added tracers are identical to BC in terms of physical properties. BAM treats BC as externally mixed with respect to other aerosol species, and hence this model is relatively unsophisticated compared with aerosol models that consider internal mixing and evolving size distributions of BC, e.g., via aerosol coating and coagulation [e.g., *Liu et al.*, 2012]. We exclude the added tracers from the radiative transfer calculations in the model, and BAM also does not treat aerosol-cloud microphysical interactions. Hence, the added tracers are climate passive and the simulated climate is exactly like the one without the added tracers. This is a necessary design feature because aerosol distributions in some of

our idealized experiments are unrealistic and would have detrimental effects on the simulated climate if they were radiatively active.

One scientific question we strive to address in this study is how much of the change in each tracer's spatial and temporal distribution under different climate scenarios can be attributed to changes in atmospheric transport pathways, and how much is caused by changes in aerosol deposition. In order to quantify the individual contributions from transport and deposition, we design two experiments to separate the change in Arctic aerosol distribution associated with those two processes. Experiment "Transport" (EXP:T) is designed so only changes in atmospheric transport affect the tracer's distribution. In EXP:T, all tracers have the same e-folding lifetime of 4 days. Both the dry and wet deposition for these tracers are disabled, so all tracers will stay in the atmosphere for exactly the same time and all changes in the tracer's distribution are caused solely by changes in atmospheric circulation. Experiment "Transport+Deposition" (EXP:T+D) is designed to consider both transport and deposition processes. In EXP:T+D, all tracers are emitted in the hydrophobic mode and convert to hydrophilic mode with an e-folding lifetime of 1.2 days, as in the default configuration of BAM. The hydrophobic tracer can only be removed by dry deposition and the hydrophilic tracer can also be removed from the atmosphere by both in-cloud and below cloud removal processes [*Rasch et al.*, 2000; *Barth et al.*, 2000]. In other words, in EXP:T+D, the parameter settings for tracer wet and dry deposition processes are the same as the default settings for BC aerosol in BAM. For both EXP:T and EXP:T+D, the model uses the CAM4 default finite volume dynamical core for tracer advection.

To compare tracer transport and deposition in changing climates, we drive the model with SST and sea-ice distributions which represent present day and future climate for both EXP:T and EXP:T+D. For present day climate we drive the model with a climatological mean annual

cycle of SSTs, averaged from 1982 to 2001. The SSTs representing future climate are averaged from the last ten years (2090 – 2099) of a CESM1 simulation with fully coupled atmosphere, ocean and land model components under the RCP8.5 forcing scenario. We denote simulations which represent present day climate by "PRD" and future climate by "RCP".

There are therefore four sets of simulations conducted for this study: EXP:T in PRD, EXP:T in RCP, EXP:T+D in PRD and EXP:T+D in RCP. In all four experiments, we simulate 200 tagged tracers which are emitted from different locations from the northern hemisphere mid-latitude land area. Figure 1 shows the emission locations for the 200 individual aerosol tracers applied in this study. All 200 tracers have the same emission rates, enabling us to easily explore the relative geographic differences in how aerosol distributions are influenced by transport and removal processes. In Section 4.3, we also include two additional tracers associated with global BC emission inventories for present day and year 2100 under the RCP8.5 scenario [*Rao and Riahi*, 2006; *Riahi et al.*, 2007, 2011]. These tracers are subject to model circulation and deposition as in EXP:T+D. The analysis in Section 4.3 enables us to quantify how the actual Arctic BC budget might change in future climate due to changes in aerosol transport and deposition processes as well as changes in emissions. In each of the experiments, we run the model for 16 years with annually repeating SSTs and sea-ice fields for present and future climatologies. The first year is used for spin-up and the remaining 15 years of simulation are used for analysis.

3. Methods

3.1. Arctic aerosol fraction

In order to quantify how effectively an aerosol tracer from a particular source location travels to (and remains within) the Arctic region (60 – 90°N), we utilize the ratio of the tracer's Arctic mean atmospheric column burden to global mean burden. We apply the term "Arctic aerosol

fraction" (AAF) to this proxy value and quantify a tracer's AAF as:

$$AAF_{Tracer} = \frac{\int_{0^\circ}^{360^\circ} \int_{60^\circ}^{90^\circ} \int_{0}^{\mathrm{TOA}} q_{Tracer}(z)\, \rho(z)\, cos(\phi)\, dz\, d\phi\, d\theta}{\int_{0^\circ}^{360^\circ} \int_{-90^\circ}^{90^\circ} \int_{0}^{\mathrm{TOA}} q_{Tracer}(z)\, \rho(z)\, cos(\phi)\, dz\, d\phi\, d\theta} \quad (1)$$

where $q_{Tracer}(z)$ is the atmospheric mass mixing ratio for that particular tracer at altitude z with unit kg kg^{-1}, $\rho(z)$ is the air density at altitude z with unit of kg m^{-3}, ϕ is latitude and θ is longitude. The AAF is unitless and simply the fraction of the aerosol tag's total global atmospheric burden that is located within the Arctic. For tracers that experience efficient transport to the Arctic, the AAF will be higher than those that experience transport barriers to the Arctic and/or have shorter atmospheric lifetimes. This quantity is utilized in the analysis of both EXP:T and EXP:T+D.

3.2. Polar dome definition

The polar dome is a boundary which separates cold air in the Arctic from the relatively warm air in mid-latitude regions. This is an important feature both for aerosol transport and as a general atmospheric phenomenon [*Klonecki et al.*, 2003; *Stohl*, 2006]. In order to quantitatively analyze the polar dome's influence on aerosol transport, we have developed a rigorous definition of the polar dome by analyzing the monthly mean 500 hPa geopotential height fields. First we calculate the latitudinal gradient of northern hemisphere 500 hPa geopotential height at all longitudes. Then we find the latitude, at each longitude, in which the geopotential height gradient is maximal. Next we take the average of the corresponding 500 hPa geopotential heights in those grid cells found above. We then locate a circumpolar isopleth based on the value calculated above and define this isopleth as the boundary of the polar dome. By this method, the polar dome is identified by the maximum zonal mean latitudinal gradient of 500 hPa geopotential height in the northern hemisphere. Logic behind this definition is that where

the latitudinal geopotential height gradient is largest, the zonal component of the geostrophic wind at that level is likely to be strongest, and this narrow band of strong geostrophic wind plays an important role for tracer transport in the middle troposphere. This narrow band of strong geostrophic wind, often referred to as the jet stream, also has a strong influence on weather systems, surface temperature, and storm tracks. The location of the polar dome and the strength of the wind speed associated with the jet stream have strong seasonal cycles. The location extends to middle latitude regions during winter and the jet wind speed reaches a maximum during this time of year. This results from the stronger temperature gradient between low and high latitude regions in winter. During summer, the location of the polar dome retreats to the north and the jet stream also weakens.

4. Results

This paper explores how warming of the climate system could influence the contributions of emissions from different regions to the Arctic via changing atmospheric transport and deposition processes. For EXP:T, we will focus our analysis primarily on January based on two reasons. First, as mentioned, the polar dome is strongest and has the most southerly extent in January, and hence changes in the dome during this season are likely to have the most pronounced impact on aerosol transport to the Arctic. Second (and related), observations show that the Arctic aerosol surface air concentrations have strong seasonality [e.g., *Sharma et al.*, 2006], with the winter months showing higher amounts and peak surface concentrations occurring in March, likely due to winter accumulation and weak winter deposition. Thus compared to summer, the winter budget of Arctic aerosol appears to be more dependent on transport processes. Although our analysis of EXP:T focuses on January, we also provide a brief discussion of a summer month (July). From analysis of climate-induced changes in tracer AAF in EXP:T+D, we will

see that aerosol deposition processes become the dominant source of change in Arctic aerosol burden, leading us to explore impacts during both winter (January) and summer (July) for this experiment. The additional BC tracers associated with realistic global BC emissions discussed in Section 4.2 and 4.3 will be used to examine the relative change in normalized tracer deposition rate (sometimes referred to as the first order removal rate) and its relationship to changes in precipitation. The annual mean Arctic budget of this set of BC tracers will also be analyzed, providing a quantitative assessment of how the Arctic BC budget would change in future climate due to changes in transport and deposition processes as well as changes in BC emissions.

4.1. Result for Experiment Transport

4.1.1. Arctic aerosol fraction

Figure 2a shows the spatial pattern of the Arctic aerosol fraction (AAF) for all of the 200 tracers in present day climate with Experiment Transport (EXP:T) in January. From Figure 2a we can see that, as expected, the AAF of tracers emitted closer to the Arctic is generally larger. The pattern also exhibits zonal asymmetries in the mid-latitudes, however, especially over Eurasia. The figure shows a trough-like structure near eastern Europe and western Asia, and the wave-like pattern is disrupted by the high Tibetan Plateau. Tracers emitted from the European continent general have higher AAF compared to the tracers emitted from East Asia in the same latitude. The pattern over North America is more symmetric. Zonal asymmetry in transport efficiency is caused by the combined effects of the location of the polar dome, which controls the middle to upper troposphere long range transport (Figure 5), differences in surface potential temperature, and variable topography that controls low level transport from the source region. Figure 2b shows the AAF pattern in future climate, and Figure 2c shows the relative change of the AAF from present day to future climate, normalized by the present day value ((RCP-

PRD)/PRD). We find that for tracers emitted from the eastern and western boundaries of the Pacific Ocean, the AAF changes substantially in future climate. Tracers emitted from East Asia have an increased Arctic fraction in the future, while the Arctic fraction for tracers emitted from North America decreases significantly. As *Koch and Hansen* [2005] and *Stohl* [2006] discovered, tracers from those two regions transport to the Arctic primarily through the middle to upper troposphere, which means they need to be lifted in the troposphere before they can be transported to the Arctic. Based on this, we try to link the change in transport to change in middle troposphere dynamics in the relevant regions.

Figure 2c indicates that emissions from different regions will experience substantially different changes in dynamical transport efficiency to the Arctic associated with warming climate. For example, the AAFs for tracers emitted from East Asia increase around 10% – 22% in future climate, and the AAFs for North American tracers decrease around 21% – 33%, due solely to changes in aerosol transport. Here we use two case studies to highlight the transport pattern shifts associated with tracers emitted from East Asia and North America, two of the largest anthropogenic emission regions in the northern hemisphere. Figure 3a depicts the distribution of tracers emitted from East Asia in January. Following emission, these tracers tend to travel in one of two directions: towards the southwest or northeast. The northeast branch is the one primarily taken by tracers contributing to the Arctic burden. Figure 3b shows the change of tracer distribution from present day to future climate, which reveals an enhanced burden of tracers over the Arctic, especially over eastern Russia and Alaska, indicating enhanced transport via the northeast branch. For tracers emitted from North America, Figure 3d shows that the Arctic burden decreases significantly in future climate.

To explore reasons for the changes shown in Figure 3, we turn to an analysis of the tracers' three dimensional distribution. Figure 4 shows the zonal mean vertical profile of tracers from East Asia, North America and Europe averaged over different latitudinal zones in January and July. The four latitudinal zones are chosen to represent mid-latitude regions and the Arctic: 32 – 42°N, 42 – 52°N, 52 – 62°N and 62 – 90°N. Figure 4a shows that tracers emitted from East Asia in January are concentrated near the surface and in the lower troposphere near the source region. The tracer moves into the higher atmosphere when it travels northward, as the mid-troposphere concentration increases while the lower atmospheric concentration decreases. When the tracer reaches the Arctic, its vertical profile (purple line) indicates the maximum concentration is located near the middle to upper troposphere (around 400 hPa to 500 hPa). This reveals that East Asian tracers travel to the Arctic mostly through the middle to upper troposphere. Combined with Figure 3a, we identify the middle to upper troposphere over northeastern Siberia, the Bering Sea and Alaska as the most important transport gateway to the Arctic for East Asian emissions. Figure 4b shows the zonal mean vertical profile of tracers emitted from North America in January. This indicates that, like the East Asian tracers, emissions from North America tend to travel to the Arctic through the middle to upper troposphere. Based on this analysis, we attribute the warming-induced change in these tracers' Arctic transport efficiencies to changes in the mid-tropospheric wind near each respective transport gateway. European emissions are also an important source of the total Arctic burden. Figure 4c shows the zonal mean vertical profile for a representative subset of European tracers in January. We can see that the tracers are concentrated near the surface and lower atmosphere throughout the source region to the Arctic. This indicates that these emissions transport to the Arctic mostly via the lower troposphere

pathways, as shown by *Stohl* [2006]. Thus these emissions are not as sensitive as the East Asian or North American tracers to changes in free troposphere dynamics.

4.1.2. Changing polar dome and its influence on aerosol transport

Before studying how the mid-troposphere wind might change between the two climate scenarios, we first exam how the winter polar dome position shifts in the future. Figure 5 shows the January mean 500 hPa geopotential height with wind vectors and the polar dome position for present (PRD), future (RCP), and their difference. From the polar dome position we can see that the wave amplitude of the dome increases over the Bering Sea and Alaska in the future. The geopotential height difference exhibits a dipole feature with a low pressure center near the central North Pacific and a high pressure center near Alaska and northwestern Canada. The net result is an enhanced northward wind component over this region at the 500 hPa level [*Francis and Vavrus*, 2012; *Lee et al.*, 2015]. From Figure 3a we can see that the East Asian tracer mixes into the Arctic over the same region where the wind shifts toward the north. This shift in the wind direction favors transport of East Asian emissions to the Arctic.

One possible explanation for the extension of the meridional amplitude of the polar dome over the Bering Sea and Alaska is inhomogeneity of Arctic warming in future climate. Under the RCP8.5 scenario, by the end of the 21st century the increase of winter surface temperature is simulated to be much stronger near the Chukchi Sea and Alaska than other regions of the Arctic, at least in this model. Figure 6a shows the surface temperature change from present day to future climate in January. The surface temperature around Chukchi Sea ranges from –10°C to –25°C in present day climate. While most of the Arctic warms by 5 – 10°C, the area near the Chukchi Sea warms by 25 – 30°C in future climate. The enhanced warming of the Chukchi Sea is associated with substantial sea ice loss in this region during winter. Figure 6b shows the change

of sea ice extent in January from present day to future climate. From the figure, we can see that the maximum sea ice loss is also in the vicinity of the Chukchi Sea. The inhomogeneity of Arctic warming and sea ice loss leads to inhomogeneity of the latitudinal temperature gradient across different longitudes. With the latitudinal temperature gradient decreasing most rapidly in the Chukchi Sea and Bering Sea region, we expect the zonal wind component of the tropospheric mid-latitude jet will become slower in this region. This, in turn, will lead to the northward extension of the polar dome boundary near the Bering Sea and Alaska.

Figure 3c shows that tracers emitted from North America primarily mix into the Arctic over the North Atlantic, Greenland and northeastern Canada. As the North American tracers also transport to the Arctic via high altitude pathways, they are sensitive to the change of wind at 500 hPa level over the North Atlantic. Figure 5c shows that the wind over the North Atlantic and northeastern Canada shifts southward in future climate. This is a net result of a high pressure anomaly over northwestern Canada and a weak low pressure anomaly over the Atlantic. The southward shift of wind inhibits the transport of North American tracers to the Arctic in future climate, opposite of the effect that occurs with East Asian tracers.

4.1.3. Seasonality of tracer transport

Figure 4d–f shows the vertical profiles of East Asia, North America and Europe tracers' mass concentration in July for EXP:T. The tracers' mass concentrations exhibit different vertical distributions than in January. This shows that in summer, aerosol emissions from all three source regions can transport to the Arctic via both the middle to high altitude pathways and also through low level transport. The relative importance of the high and low pathways are different in summer, however. The high altitude transport is still dominant for Arctic transport of East Asian and North American emissions. The altitude of maximum mass mixing ratio in

the Arctic for East Asian and North American tracers elevates about 2800 m in comparison with January. For the European tracer, the Arctic mass mixing ratio also shows a maximum at high altitude, indicating high level transport from the source region. This change is caused by enhanced convection during summer, different potential temperatures between emission and receptor regions, and weakening of the polar dome and jet stream in summer [*Koch and Hansen*, 2005; *Stohl*, 2006]. Figure 4d–f shows similar changes in Arctic burden for tracers emitted from East Asia, North America and Europe between present day and future climates. For tracers emitted during summer from East Asia, both the high and low portions of the Arctic atmosphere show increased mass mixing ratios in a warming climate. Meanwhile, we see decreased Arctic mixing ratios for North American tracers, and increased mixing ratios from European tracers.

4.2. Results for Experiment Transport+Deposition

4.2.1. Arctic aerosol fraction

The previous section showed that changing atmospheric dynamics associated with climate change have varying impacts on tracer transport to the Arctic. Another critical factor influencing the tracers' spatial and temporal distributions is the deposition process. In this section, we will use the same model framework to represent present day and future climates, but will use active wet and dry deposition for tracer removal processes. In EXP:T+D, the tracer is subject to the wet and dry deposition processes that it experiences during its atmospheric life cycle. The treatments of the wet and dry deposition for all the 200 tracers in this experiment are the same as the default settings for BC in BAM [*Rasch et al.*, 2000; *Barth et al.*, 2000]. The SST and sea-ice distributions for present day and future climate representations are the same as EXP:T.

Figure 7a shows the spatial pattern of the January Arctic aerosol fraction (AAF) in EXP:T+D, for all of the 200 tracers in present day climate. Figure 7a reveals that the pattern of tracers' AAF

with active wet and dry deposition is very similar to that produced with constant aerosol lifetime in EXP:T. Figure 7b shows the AAF pattern for EXP:T+D in future climate. The general AAF pattern structure does not show dramatic changes from PRD to RCP, but the relative changes in Arctic aerosol fraction between the two climate scenarios are substantial, as shown in Figure 7c. From Figure 7c, we find that the AAF decreases significantly with climate warming for tracers emitted from almost the entire northern hemisphere mid-latitude land mass, except for a few regions in western Europe and southern Alaska. Emissions from the central and eastern parts of North America experience the strongest decreases in AAF. About 70% less of the tracers emitted from this region reside in the Arctic in future climate. This is caused by the net effects of decreasing Arctic transport as revealed by EXP:T, and increasing Arctic deposition efficiency in a warmer and wetter climate (Section 4.2.2). Meanwhile, for emissions from the west coast of North America, most of East Asia and Central Asia, and eastern Europe, the decrease in AAF is significant but not as substantial as that associated with emissions from central and eastern North America. This suggests that the effect on aerosol burden of more rapid Arctic deposition is partially offset by the enhanced northward transport of these emissions in future climate. The decreases in AAF for tracers emitted from most parts of Europe, Asia and western North America range from 20% to 50% in future climate.

4.2.2. Influence of tracer deposition

The distinct difference between the results from EXP:T and EXP:T+D indicates that changes in deposition are the dominant drivers of changes in the tracer burdens with 21st century climate change. The purpose of this section is to investigate the relative changes in deposition *efficiency* from present day to future climate, as a means of identifying the regions along transport pathways that are responsible for enhanced deposition and therefore reduced Arctic aerosol

burdens. Here we shift to using the additional tracer in EXP:T+D that has a simulated distribution associated with realistic BC emissions from year 2000. This tracer applies the year 2000 BC emission inventory developed with RCP8.5 scenario, with annual global emission of 7.5 Tg [*Rao and Riahi*, 2006; *Riahi et al.*, 2007, 2011]. We refer to this tracer as the realistic BC tracer to distinguish it from the 200 tagged tracers analyzed in previous sections. The realistic BC tracer is subject to the same aerosol treatment as the other tagged tracers in EXP:T+D, and we use the same emission inventory in the present and future simulations presented here. As we focus here on the spatial distributions of relative changes in deposition efficiency, we are able to simply use a single global BC tracer, while retaining realistic spatial heterogeneity of BC emissions.

We use the tracer's first-order removal rate as a measure of the deposition efficiency. The first-order removal rate is defined as the tracer's total deposition rate normalized by its column burden [e.g., *Wang et al.*, 2013]. This term reflects the tracer's atmospheric removal efficiency and has units of day^{-1}. Figure 8b shows the relative differences in the realistic BC tracer's first-order removal rate between present day and future climates in January. In the northern hemisphere, the largest relative increases in first-order removal rate are located in the Arctic and near the eastern shore of the Pacific. The Arctic mean first-order removal rate increases by 23.3% in January. This indicates that reduced Arctic aerosol burden in future climate is due more to faster removal of aerosols from the Arctic atmosphere than from reduced transport to the Arctic. This pattern is a direct result of the precipitation changes in future climate. Figure 9b shows the relative change in total precipitation rate from present to future climates in January. We can see that in the regions where the relative increases in precipitation are large (like the Arctic and eastern Pacific), the tracers' deposition efficiency is also substantially enhanced. This is consistent

with the fact that the majority of the tracer's removal is associated with wet deposition [e.g., *Garrett et al.*, 2010]. As the Arctic removal process accelerates in future climate, the tracer's Arctic residence time and mean burden will tend to decrease. Thus, even though atmospheric circulation changes favor enhanced transport of East Asian emissions to the Arctic, the Arctic burden of these emissions will decrease due to the larger offsetting effect of increased deposition efficiency in the Arctic. By comparing the results of these two experiments, we can qualitatively state that aerosol wet deposition processes dominate the change in Arctic aerosol burden with anthropogenic climate warming.

4.2.3. Seasonality of changes in tracer transport and deposition

In EXP:T+D deposition becomes the dominant source of decreased AAF with climate change during winter. In July, the relative change in Arctic deposition efficiency is weaker compared to winter. From Figure 8c, we see that the first-order removal rate during July is enhanced near the Chukchi Sea and the east of Greenland, while decreasing over the west of Greenland and other regions in the Arctic. The regions that show substantial first-order removal rate changes in July also have large changes in precipitation rate, as depicted in Figure 9c. In July, the future mean Arctic first-order removal rate for the realistic BC tracer increases about 2.0% compared to present day climate.

4.3. Change in the Arctic BC distribution in future climate

4.3.1. Change in BC emission in future climate

In this section, we quantify changes in the Arctic BC budget in future climate due to changes in transport and deposition, as well as changes in BC emissions. We apply model settings as in EXP:T+D with two additional tracers. One tracer represents the present day BC emission inventory (Ep) under the RCP8.5 scenario for year 2000 [*Rao and Riahi*, 2006; *Riahi et al.*,

2007, 2011]. We simulate the distribution of this tracer both under present climate (EpCp) as well as future climate (EpCf). The relative changes $[(EpCf - EpCp)/EpCp]$ of this tracer's column burden inform on how the BC distribution will change solely due to changes in transport and deposition. A second tracer tracks a projected future emission inventory simulated in the presence of future climate (EfCf). The future emission inventory applies year 2100 BC emissions developed for RCP8.5 [*Rao and Riahi*, 2006; *Riahi et al.*, 2007, 2011]. Table 1 shows the total annual global and Arctic emissions for these present day and future inventories. From Table 1, we can see the global annual BC emissions decrease by about 43.5% by the end of 21st century as projected by the RCP8.5 scenario. The BC emissions from 60°N to 90°N in this inventory decrease by 21.7%, but may not include realistic changes in Arctic shipping and flaring [*Corbett et al.*, 2010; *Stohl et al.*, 2013]. The relative changes between EfCf and EpCp will help us quantify how the changes in emissions associated with economic and policy scenarios for the future will affect the BC distribution.

4.3.2. Net change of Arctic BC distribution

Figure 10 shows the relative change of the annual mean BC column burden between experiments EpCp and EpCf (panel a), and between experiments EpCp and EfCf (panel b). In both cases, there are strong reductions in the Arctic burden in future climate, though the changes are much larger when future emissions are also included. As discussed in Section 4.2.2, changes in deposition are a much larger contributor to the changes in Arctic aerosol distribution in future climate than changes in transport. Here we notice that regions which show large reductions in the BC column burden (Figure 10a) also show substantial increases in the first order removal rate (Figure 8a). Table 1 shows that the annual mean Arctic BC column burden averaged over 60°N to 90°N decreases by 13.6% by the end of 21st century between EpCp and EpCf. Yet

the change of annual mean Arctic BC deposition flux is only 0.7% between EpCp and EpCf. It indicates that in a warming climate, the annual mean BC deposition flux to the Arctic surface does not change much if the emission does not change. The increase of deposition efficiency in future climate is a more important contributor to the reduction of Arctic BC column burden other than changes in aerosol transport.

In previous sections, we showed that aerosol transport and deposition efficiencies both change in the future due to climate warming. Meanwhile, emissions will also continue to change with technological and economic developments. For example, the total global annual BC emissions decline from 7.52 Tg in 2000 to 4.25 Tg in 2100 in the RCP8.5 inventories. The reduction in BC emissions will also influence the global and Arctic BC budget. Figure 10b shows the relative change in BC column burden between experiments EfCf and EpCp, indicating dramatic decreases in the future when reduced BC emissions are also accounted for. The annual mean Arctic BC column burden averaged over 60°N to 90°N decreases 61.0% by the end of the 21st century due to changes in transport, deposition, and emissions. Figure 11 shows seasonal average of Arctic BC column burden for experiments EpCp, EpCf and EfCf. For the climate-induced changes in Arctic BC (difference between EpCp and EpCf), we notice that the reduction of Arctic BC column burden is most significant in fall and winter months because the increase of aerosol removal efficiency peaks during these seasons.

5. Conclusion

In this study, firstly, we use simulations with 200 tagged black carbon-like tracers in the Community Atmosphere Model version 4 (CAM4) to explore changes in atmospheric transport and deposition processes in the context of global climate change. We find that the poleward tracer transport efficiency for aerosols emitted during winter from East Asia will increase by

about 10% – 22% in a warming climate. In particular, the meridional amplitude of the polar dome over the central and eastern Pacific will extend due to inhomogeneity in Arctic warming. This will cause the mid-tropospheric winds to shift north over the Pacific, favoring poleward transport of East Asian aerosol emissions. Meanwhile, as the mid-tropospheric wind shifts to the south over the North Atlantic and Greenland, tracers emitted from North America will experience decreased transport efficiency to the Arctic.

When we consider the combined effects of changes in transport and deposition processes, however, we find that deposition is the dominant process affecting the future Arctic tracer budget. The Arctic aerosol fraction (AAF, defined as a tracer's total Arctic burden divided by its global burden) for tracers emitted from East Asia and North America will decrease significantly in a warming climate due to more efficient wet removal in the Arctic. This results from enhanced precipitation in the Arctic, especially during winter. In simulations with present-day emissions of black carbon, enhanced wet removal reduces the Arctic annual mean black carbon column burden by 13.6% by the end of 21st century. Biases related to simulated precipitation fields and lack of aerosol – cloud interactions in this version of the model contribute to uncertainties in this analysis. Yet the relative changes derived here are consistent with multiple lines of reasonings and can serve as estimations of projected future scenarios. Reduced BC emissions will likely lead to a further decrease in the Arctic black carbon burden, however, and are the leading cause of reduced Arctic BC under the RCP8.5 scenario. A simulation with combined climate changes and emissions changes under RCP8.5 shows the Arctic annual mean BC column burden decreasing by 61.0% by the end of 21st century.

Acknowledgments. We thank Justin Perket for providing us with SST data from future climate simulations. This work was supported by NSF grants ATM-0852775 and ARC-1253154.

The scripts and files necessary to reproduce the experiments with Community Earth System Model version 1.1.1 (CESM1.1.1), as well as the model output data used for this study, are available from the authors upon request (chaoyij@umich.edu). The scripts and data are archived on a workstation owned by the University of Michigan.

References

Barth, M. C., P. J. Rasch, J. T. Kiehl, C. M. Benkovitz, and S. E. Schwartz (2000), Sulfur chemistry in the National Center for Atmospheric Research Community Climate Model: Description, evaluation, features, and sensitivity to aqueous chemistry, *J. Geophys. Res.*, *105*(D1), 1387–1415.

Bintanja, R., and E. C. van der Linden (2013), The changing seasonal climate in the Arctic, *Nature*, *3*(1556), doi:10.1038/srep01556.

Bond, T. C., S. J. Doherty, D. W. Fahey, P. M. Forster, T. Berntsen, B. J. DeAngelo, M. G. Flanner, S. Ghan, B. Kärcher, D. Koch, S. Kinne, Y. Kondo, P. K. Quinn, M. C. Sarofim, M. G. Schultz, M. Schulz, C. Venkataraman, H. Zhang, S. Zhang, N. Bellouin, S. K. Guttikunda, P. K. Hopke, M. Z. Jacobson, J. W. Kaiser, Z. Klimont, U. Lohmann, J. P. Schwarz, D. Shindell, T. Storelvmo, S. G. Warren, and C. S. Zender (2013), Bounding the role of black carbon in the climate system: A scientific assessment, *J. Geophys. Res. Atmos.*, *118*, 5380–5552, doi:10.1002/jgrd.50171.

Browse, J., K. S. Carslaw, A. Schmidt, and J. J. Corbett (2013), Impact of future Arctic shipping on high-latitude black carbon deposition, *Geophys. Res. Lett.*, *40*(16), 4459–4463, doi:10.1002/grl.50876.

Corbett, J. J., D. A. Lack, J. J. Winebrake, S. Harder, J. A. Silberman, and M. Gold (2010), Arctic shipping emissions inventories and future scenarios, *Atmos. Chem. Phys.*, *10*(19), 9689–9704, doi:10.5194/acp-10-9689-2010.

Eckhardt, S., B. Quennehen, D. J. L. Olivié, T. K. Berntsen, R. Cherian, J. H. Christensen, W. Collins, S. Crepinsek, N. Daskalakis, M. Flanner, A. Herber, C. Heyes, Ø. Hodnebrog, L. Huang, M. Kanakidou, Z. Klimont, J. Langner, K. S. Law, M. T. Lund, R. Mahmood, A. Massling, S. Myriokefalitakis, I. E. Nielsen, J. K. Nøjgaard, J. Quaas, P. K. Quinn, J.-C. Raut, S. T. Rumbold, M. Schulz, S. Sharma, R. B. Skeie, H. Skov, T. Uttal, K. von Salzen, and A. Stohl (2015), Current model capabilities for simulating black carbon and sulfate concentrations in the arctic atmosphere: a multi-model evaluation using a comprehensive measurement data set, *Atmospheric Chemistry and Physics*, *15*(16), 9413–9433, doi:10.5194/acp-15-9413-2015.

Flanner, M. G., C. S. Zender, J. T. Randerson, and P. J. Rasch (2007), Present day climate forcing and response from black carbon in snow, *J. Geophys. Res.*, *112*, D11202, doi:10.1029/2006JD008003.

Francis, J. A., and S. J. Vavrus (2012), Evidence linking Arctic amplification to extreme weather in mid-latitudes, *Geophys. Res. Lett.*, *39*(6), doi:10.1029/2012GL051000.

Garrett, T. J., C. Zhao, and P. C. Novelli (2010), Assessing the relative contributions of transport efficiency and scavenging to seasonal variability in Arctic aerosol, *Tellus*, *62B*, 190–196, doi:10.1111/j.1600-0889.2010.00453.x.

Garrett, T. J., S. Brattström, S. Sharma, D. E. Worthy, and P. Novelli (2011), The role of scavenging in the seasonal transport of black carbon and sulfate to the arctic, *Geophys. Res. Lett.*, *38*(16), L16805, doi:10.1029/2011GL048221.

Gent, P. R., G. Danabasoglu, L. J. Donner, M. M. Holland, E. C. Hunke, S. R. Jayne, D. M. Lawrence, R. B. Neale, P. J. Rasch, M. Vertenstein, et al. (2011), The community climate system model version 4, *Journal of Climate*, *24*(19), 4973–4991.

Holland, M. M., and C. M. Bitz (2003), Polar amplification of climate change in coupled models, *Climate Dyn.*, *21*, 221–232, doi:10.1007/s00382-003-0332-6.

Klonecki, A., P. Hess, L. Emmons, L. Smith, J. Orlando, and D. Blake (2003), Seasonal changes in the transport of pollutants into the arctic troposphere-model study, *Journal of Geophysical Research: Atmospheres*, *108*(D4), n/a–n/a, doi:10.1029/2002JD002199.

Koch, D., and J. Hansen (2005), Distant origins of Arctic black carbon: A Goddard Institute for Space Studies ModelE experiment, *J. Geophys. Res.*, *110*, D04204, doi:10.1029/2004JD005296.

Koch, D., M. Schulz, S. Kinne, C. McNaughton, J. R. Spackman, Y. Balkanski, S. Bauer, T. Berntsen, T. C. Bond, O. Boucher, M. Chin, A. Clarke, N. De Luca, F. Dentener, T. Diehl, O. Dubovik, R. Easter, D. W. Fahey, J. Feichter, D. Fillmore, S. Freitag, S. Ghan, P. Ginoux, S. Gong, L. Horowitz, T. Iversen, A. Kirkevåg, Z. Klimont, Y. Kondo, M. Krol, X. Liu, R. Miller, V. Montanaro, N. Moteki, G. Myhre, J. E. Penner, J. Perlwitz, G. Pitari, S. Reddy, L. Sahu, H. Sakamoto, G. Schuster, J. P. Schwarz, Ø. . Seland, P. Stier, N. Takegawa, T. Takemura, C. Textor, J. A. van Aardenne, and Y. Zhao (2009), Evaluation of black carbon estimations in global aerosol models, *Atmospheric Chemistry and Physics*, *9*(22), 9001–9026, doi:10.5194/acp-9-9001-2009.

Lamarque, J.-F., T. C. Bond, V. Eyring, C. Granier, A. Heil, Z. Klimont, D. Lee, C. Liousse, A. Mieville, B. Owen, M. G. Schultz, D. Shindell, S. J. Smith, E. Stehfest, J. Van Aardenne, O. R. Cooper, M. Kainuma, N. Mahowald, J. R. McConnell, V. Naik, K. Riahi, and

553 D. P. van Vuuren (2010), Historical (1850–2000) gridded anthropogenic and biomass burning
554 emissions of reactive gases and aerosols: methodology and application, *Atmos. Chem. Phys.*,
555 *10*(15), 7017–7039, doi:10.5194/acp-10-7017-2010.

556 Lamarque, J.-F., G. Kyle, M. Meinshausen, K. Riahi, S. Smith, D. van Vuuren, A. Conley,
557 and F. Vitt (2011), Global and regional evolution of short-lived radiatively-active gases and
558 aerosols in the representative concentration pathways, *Climatic Change*, *109*(1-2), 191–212,
559 doi:10.1007/s10584-011-0155-0.

560 Lamarque, J.-F., L. K. Emmons, P. G. Hess, D. E. Kinnison, S. Tilmes, F. Vitt, C. L. Heald,
561 E. A. Holland, P. H. Lauritzen, J. Neu, J. J. Orlando, P. J. Rasch, and G. K. Tyndall
562 (2012), Cam-chem: description and evaluation of interactive atmospheric chemistry in the
563 community earth system model, *Geoscientific Model Development*, *5*(2), 369–411, doi:
564 10.5194/gmd-5-369-2012.

565 Law, K. S., and A. Stohl (2007), Arctic air pollution: Origins and impacts, *Science*, *315*, 1537–
566 1540.

567 Lee, M.-Y., C.-C. Hong, and H.-H. Hsu (2015), Compounding effects of warm sea surface
568 temperature and reduced sea ice on the extreme circulation over the extratropical north pacific
569 and north america during the 2013”2014 boreal winter, *Geophysical Research Letters*, *42*(5),
570 1612–1618, doi:10.1002/2014GL062956.

571 Lee, Y. H., J.-F. Lamarque, M. G. Flanner, C. Jiao, D. T. Shindell, T. Berntsen, M. M. Bisi-
572 aux, J. Cao, W. J. Collins, M. Curran, R. Edwards, G. Faluvegi, S. Ghan, L. W. Horowitz,
573 J. R. McConnell, J. Ming, G. Myhre, T. Nagashima, V. Naik, S. T. Rumbold, R. B. Skeie,
574 K. Sudo, T. Takemura, F. Thevenon, B. Xu, and J.-H. Yoon (2013), Evaluation of prein-
575 dustrial to present-day black carbon and its albedo forcing from atmospheric chemistry and

576 climate model intercomparison project (accmip), *Atmospheric Chemistry and Physics*, *13*(5),
577 2607–2634, doi:10.5194/acp-13-2607-2013.

578 Liu, J., S. Fan, L. W. Horowitz, and H. Levy II (2011), Evaluation of factors controlling long-
579 range transport of black carbon to the Arctic, *J. Geophys. Res.*, *116*(D4), D04307, doi:10.
580 1029/2010JD015145.

581 Liu, X., R. C. Easter, S. J. Ghan, R. Zaveri, P. Rasch, X. Shi, J.-F. Lamarque, A. Gettelman,
582 H. Morrison, F. Vitt, A. Conley, S. Park, R. Neale, C. Hannay, A. M. L. Ekman, P. Hess,
583 N. Mahowald, W. Collins, M. J. Iacono, C. S. Bretherton, M. G. Flanner, and D. Mitchell
584 (2012), Toward a minimal representation of aerosols in climate models: description and eval-
585 uation in the Community Atmosphere Model CAM5, *Geosci. Model Dev.*, *5*(3), 709–739,
586 doi:10.5194/gmd-5-709-2012.

587 Ma, P.-L., J. R. Gattiker, X. Liu, and P. J. Rasch (2013), A novel approach for determining
588 source–receptor relationships in model simulations: a case study of black carbon transport in
589 northern hemisphere winter, *Environmental Research Letters*, *8*(2), 024,042.

590 Ramanathan, V., and G. Carmichael (2008), Global and regional climate changes due to black
591 carbon, *Nature Geosci.*, *1*, 221–227.

592 Rao, S., and K. Riahi (2006), The role of non-co2 greenhouse gases in climate change mitiga-
593 tion: Long-term scenarios for the 21st century, *The Energy Journal*, *27*, 177–200.

594 Rasch, P. J., M. C. Barth, J. T. Kiehl, S. E. Schwartz, and C. M. Benkovitz (2000), A description
595 of the global sulfur cycle and its controlling processes in the National Center for Atmospheric
596 Research Community Climate Model, *J. Geophys. Res.*, *105*, 1367–1385.

597 Riahi, K., A. Grbler, and N. Nakicenovic (2007), Scenarios of long-term socio-economic and
598 environmental development under climate stabilization, *Technological Forecasting and Social*

599 *Change*, *74*(7), 887 – 935, doi:http://dx.doi.org/10.1016/j.techfore.2006.05.026, greenhouse
600 Gases - Integrated Assessment.
601 Riahi, K., S. Rao, V. Krey, C. Cho, V. Chirkov, G. Fischer, G. Kindermann, N. Nakicenovic,
602 and P. Rafaj (2011), Rcp 8.5"a scenario of comparatively high greenhouse gas emissions,
603 *Climatic Change*, *109*(1-2), 33–57, doi:10.1007/s10584-011-0149-y.
604 Screen, J. A., and I. Simmonds (2010), The central role of diminishing sea ice in recent Arctic
605 temperature amplification, *Nature*, *464*, 1334–1337, doi:10.1038/nature09051.
606 Screen, J. A., C. Deser, and I. Simmonds (2012), Local and remote controls on observed Arctic
607 warming, *Geophys. Res. Lett.*, *39*(10), L10709, doi:10.1029/2012GL051598.
608 Serreze, M. C., A. P. Barrett, J. C. Stroeve, D. N. Kindig, and M. M. Holland (2009), The
609 emergence of surface-based arctic amplification, *The Cryosphere*, *3*(1), 11–19.
610 Sharma, S., E. Andrews, L. A. Barrie, J. A. Ogren, and D. Lavoue (2006), Variations and sources
611 of the equivalent black carbon in the High Arctic revealed by long term observations at Alert
612 and Barrow: 1989–2003, *J. Geophys. Res*, *111*, D14208, doi:10.1029/2005JD006581.
613 Shindell, D. T., M. Chin, F. Dentener, R. M. Doherty, G. Faluvegi, A. M. Fiore, P. Hess,
614 D. M. Koch, I. A. MacKenzie, M. G. Sanderson, M. G. Schultz, M. Schulz, D. S. Stevenson,
615 H. Teich, C. Textor, O. Wild, D. J. Bergmann, I. Bey, H. Bian, C. Cuvelier, B. N. Duncan,
616 G. Folberth, L. W. Horowitz, J. Jonson, J. W. Kaminski, E. Marmer, R. Park, K. J. Pringle,
617 S. Schroeder, S. Szopa, T. Takemura, G. Zeng, T. J. Keating, and A. Zuber (2008), A multi-
618 model assessment of pollution transport to the Arctic, *Atmos. Chem. Phys.*, *8*, 5353–5372,
619 doi:10.5194/acp-8-5353-2008.
620 Stohl, A. (2006), Characteristics of atmospheric transport into the Arctic troposphere, *J. Geo-*
621 *phys. Res.*, *111*, D11306, doi:10.1029/2005JD006888.

Stohl, A., Z. Klimont, S. Eckhardt, K. Kupiainen, V. P. Shevchenko, V. M. Kopeikin, and A. N. Novigatsky (2013), Black carbon in the arctic: the underestimated role of gas flaring and residential combustion emissions, *Atmospheric Chemistry and Physics*, *13*(17), 8833–8855, doi:10.5194/acp-13-8833-2013.

Wang, H., R. C. Easter, P. J. Rasch, M. Wang, X. Liu, S. J. Ghan, Y. Qian, J.-H. Yoon, P.-L. Ma, and V. Vinoj (2013), Sensitivity of remote aerosol distributions to representation of cloud–aerosol interactions in a global climate model, *Geosci. Model Dev.*, *6*(3), 765–782, doi:10.5194/gmd-6-765-2013.

Wang, H., P. J. Rasch, R. C. Easter, B. Singh, R. Zhang, P.-L. Ma, Y. Qian, S. J. Ghan, and N. Beagley (2014), Using an explicit emission tagging method in global modeling of source-receptor relationships for black carbon in the arctic: Variations, sources, and transport pathways, *Journal of Geophysical Research: Atmospheres*, *119*(22), 12,888–12,909, doi:10.1002/2014JD022297.

Wang, Q., D. J. Jacob, J. A. Fisher, J. Mao, E. M. Leibensperger, C. C. Carouge, P. Le Sager, Y. Kondo, J. L. Jimenez, M. J. Cubison, and S. J. Doherty (2011), Sources of carbonaceous aerosols and deposited black carbon in the Arctic in winter–spring: implications for radiative forcing, *Atmos. Chem. Phys.*, *11*(23), 12,453–12,473, doi:10.5194/acp-11-12453-2011.

Zhou, C., J. E. Penner, M. G. Flanner, M. M. Bisiaux, R. Edwards, and J. R. McConnell (2012), Transport of black carbon to polar regions: Sensitivity and forcing by black carbon, *Geophysical Research Letters*, *39*(22), n/a–n/a, doi:10.1029/2012GL053388.

Figure 1. The emission locations of the 200 tagged aerosol tracers are indicated by each individual box with grey shading in this figure.

Figure 2. Contour plot of January Arctic aerosol fraction (AAF) of the 200 tracers for (a): present-day (PRD) climate, (b): end of 21st century climate (RCP8.5), and (c): the relative change between RCP and PRD ((RCP-PRD)/PRD). Relative changes significant at the $\alpha < 0.05$ level, determined with the Wilcoxon rank-sum test, are shown with cross signs.

Figure 3. Tracer column burden distributions in EXP:T during January for (a): East Asian tracer emissions in present day climate, (b): the difference in column burden between future and present day climate (RCP–PRD) for East Asian emissions, (c): the same as (a) but for North American tracers, and (d): the same as (b) but for North American tracers. Figures show the region between 15°N to 90°N, and the bold black line indicates the 60°N circle.

Figure 4. Vertical profile of zonally averaged concentration of (a): East Asian tracers in January, (b): North American tracers in January, (c): European tracers in January, (d): East Asian tracers in July, (e): North American tracers in July, and (f): European tracers in July.

Figure 5. The 15-year mean January 500 hPa geopotential height and wind (units of m/s) for (a): present-day, (b): future, and (c): their difference (future – present). The bold blue and red lines depict the mean positions of the polar dome in present and future climate, respectively.

Figure 6. (a) January surface temperature difference between future and present climate (RCP–PRD) and (b) January Arctic sea ice extent difference (RCP–PRD). Figures show the region between 30°N to 90°N, and the bold black line indicates the 60°N circle.

Figure 7. The same as Fig. 2 but for EXP:T+D (active transport and deposition).

Figure 8. Relative change in the first order removal rate from present day to future climates ((RCP-PRD)/PRD) for present-day BC emissions during (a): annual mean, (b): January, and (c): July. Figures show the region between 45°N to 90°N, and the bold black line indicates the 60°N circle.

Figure 9. Relative change in the total precipitation rate (convective and stratiform) from present day to future climates ((RCP-PRD)/PRD) averaged over 15 years for (a): annual mean, (b): January, and (c): July. Figures show the region between 45°N to 90°N, and the bold black line indicates the 60°N circle.

Table 1. Total annual global and Arctic BC emissions for present day and future emission inventories. Annual mean global and Arctic BC column burden, and Arctic deposition flux in simulations for present day emission with present day climate (EpCp), present day emission with future climate (EpCf) and future emission with future climate (EfCf).

Experiment	Global emission (Tg)	Arctic emission (kg)	Global mean column burden ($kg\,m^{-2}$)	Arctic mean column burden ($kg\,m^{-2}$)	Arctic m flux (kg
EpCp	7.52	5.49×10^{7}	2.24×10^{-7}	1.25×10^{-7}	2.7
EpCf	7.52	5.49×10^{7}	2.25×10^{-7}	1.08×10^{-7}	2.7
EfCf	4.25	4.30×10^{7}	1.35×10^{-7}	4.88×10^{-8}	9.5

Figure 10. Relative change in the column burden of black carbon from present day to future climates simulated with: (a) present day emission inventory in both present day and future climates simulation (EpCf-EpCp)/EpCp, and (b) present day and projected future emission inventory for corresponding climate scenarios (EfCf-EpCp)/EpCp. Figures show the region between 45°N to 90°N, and the bold black line indicates 60°N circle.

Figure 11. Seasonality of Arctic mean BC column burden averaged over 60°N to 90°N for experiments: EpCp, EpCf and EfCf.

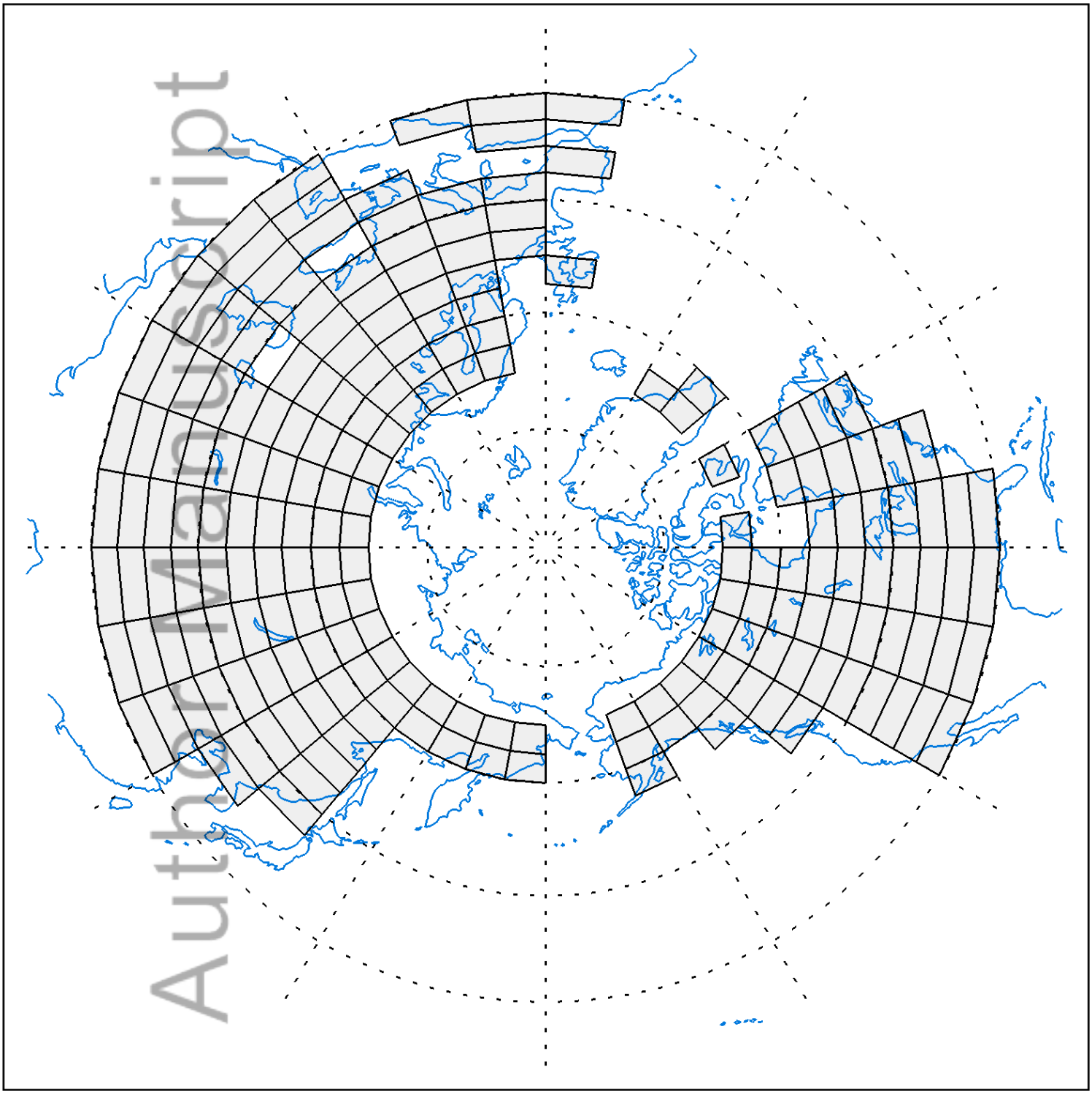

2015JD023964-f01-z-.png

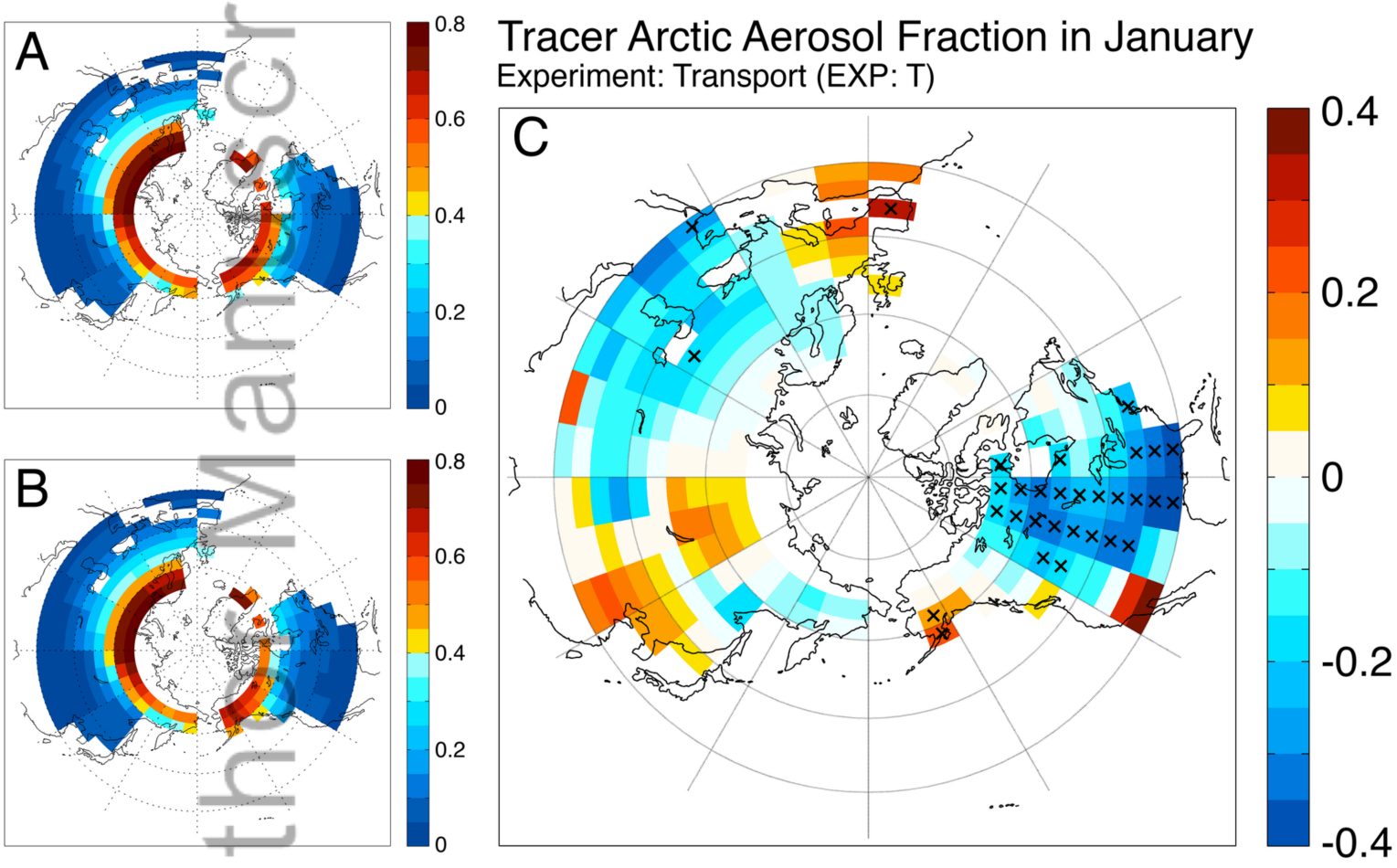

2015JD023964-f02-z-.png

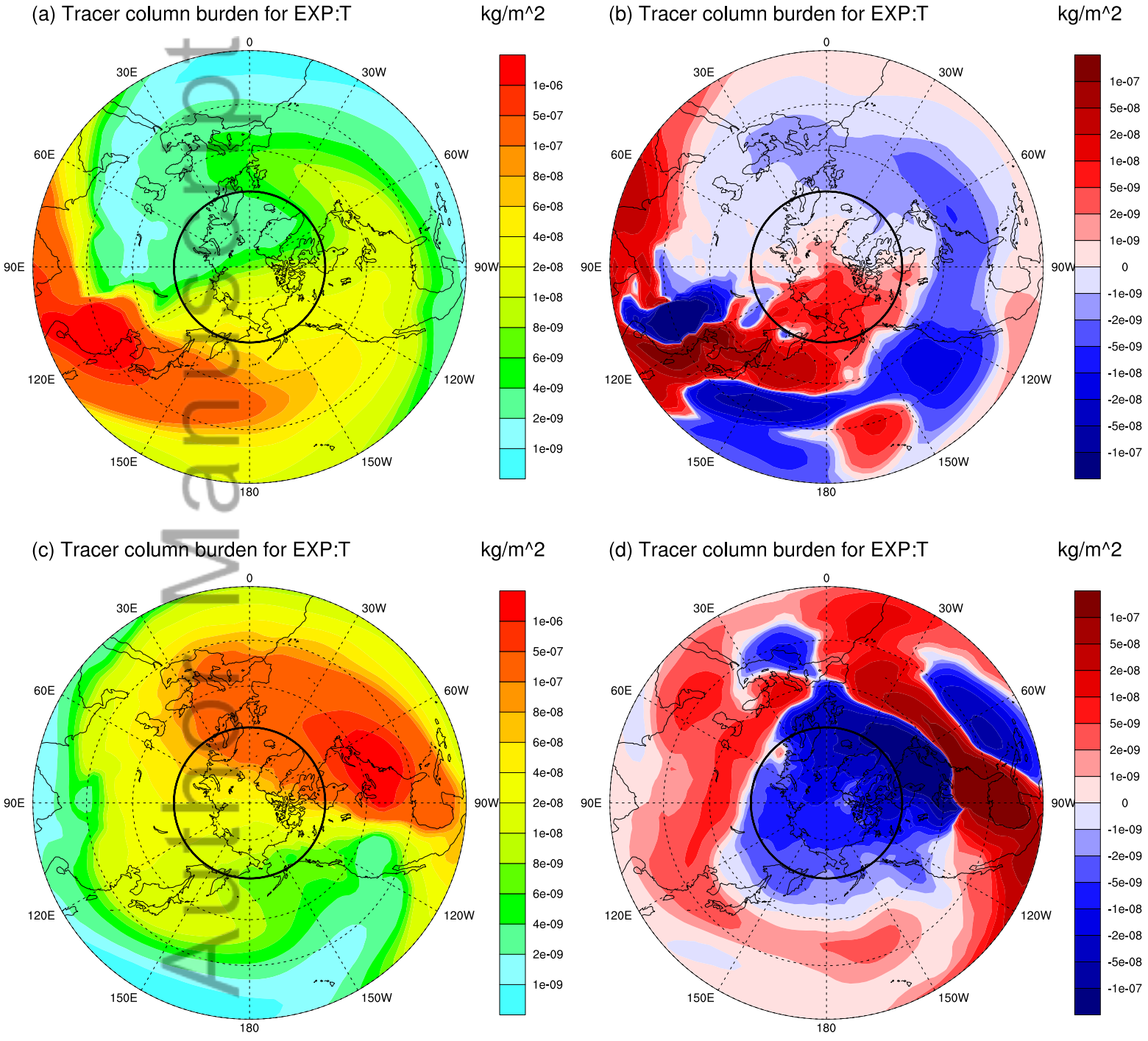

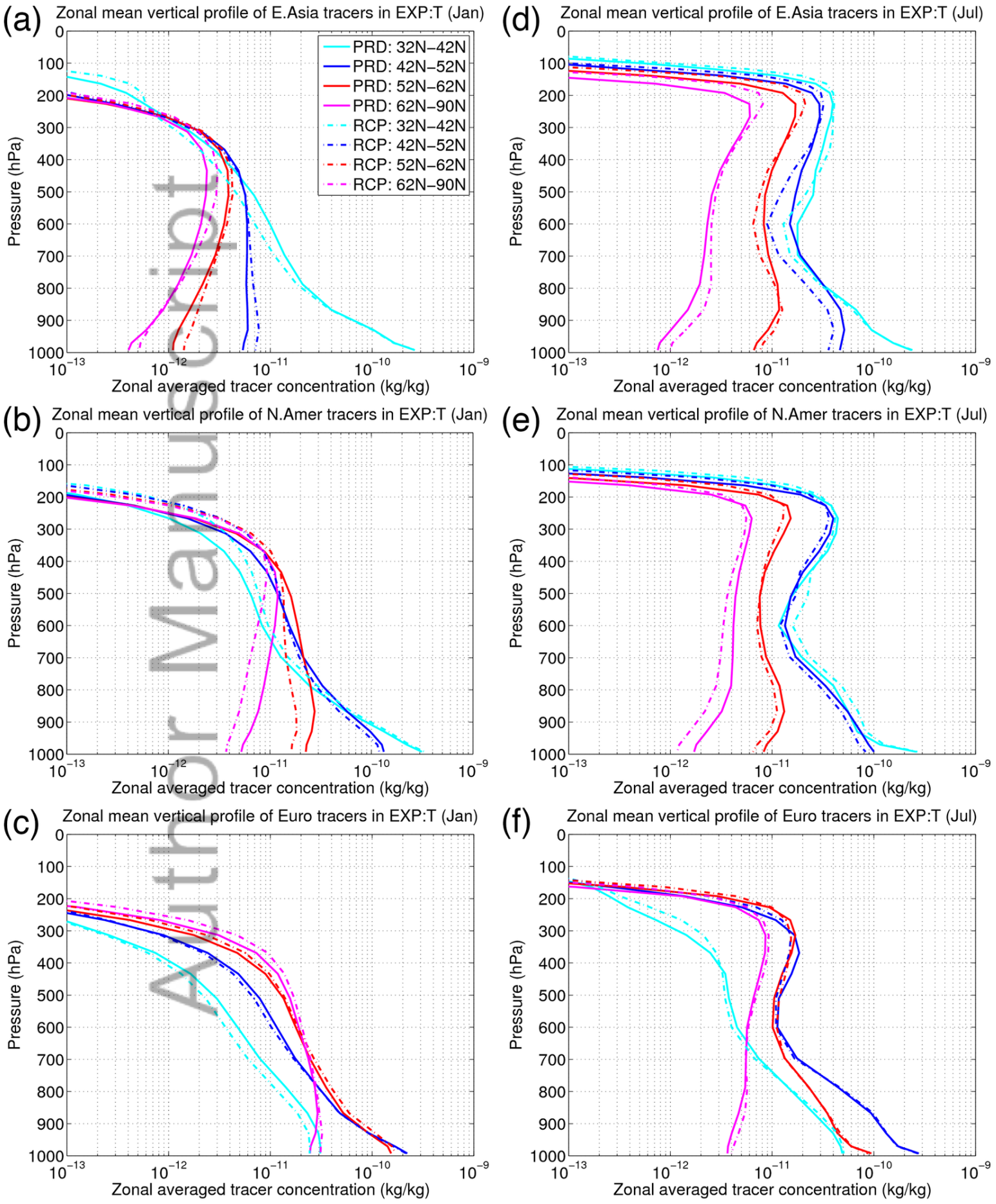

2015JD023964-f04-z-.png

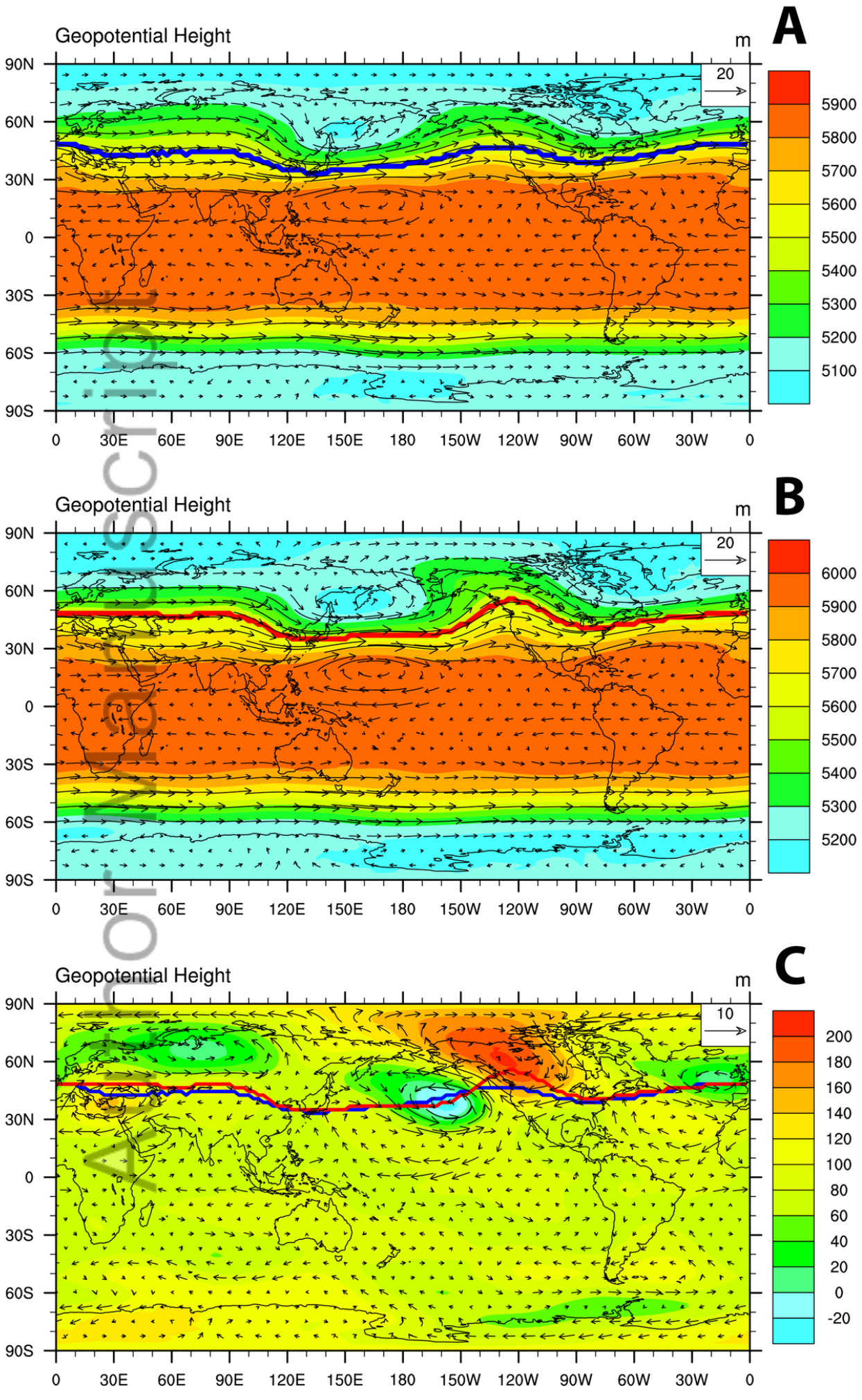

2015JD023964-f05-z-.png

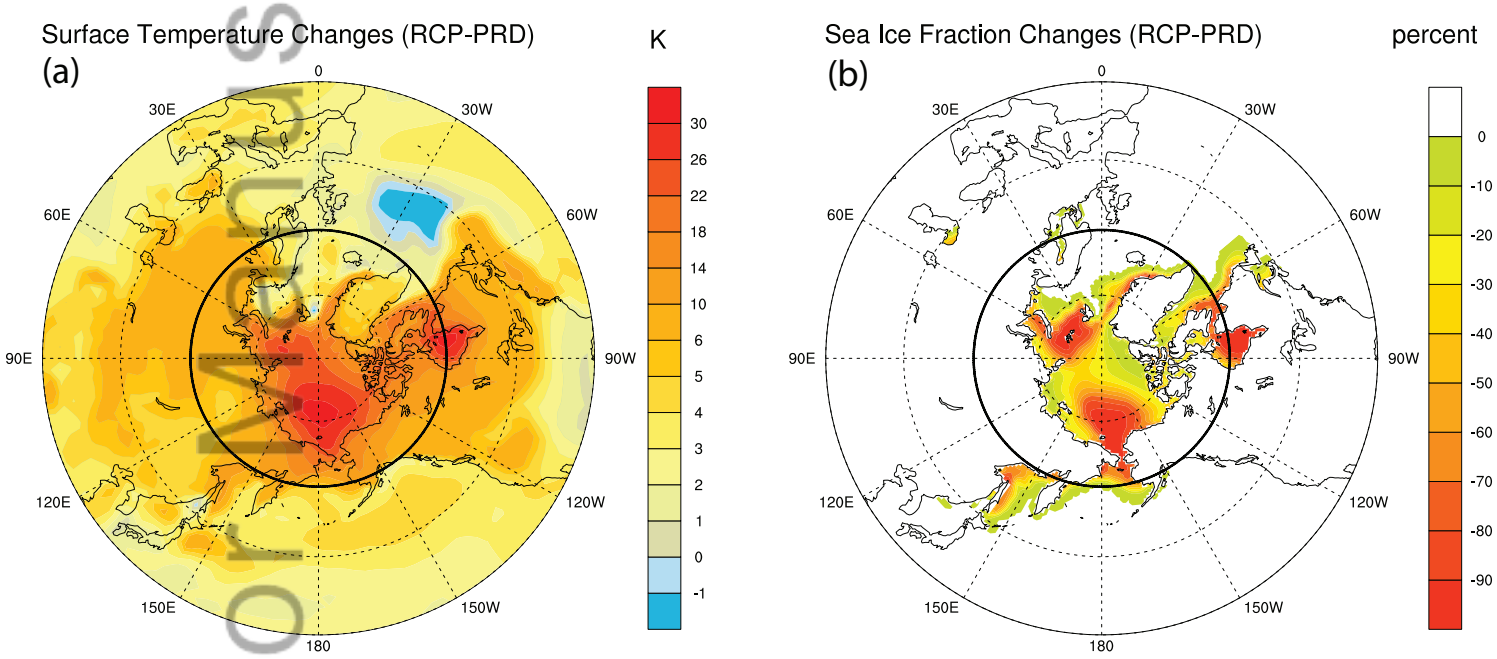

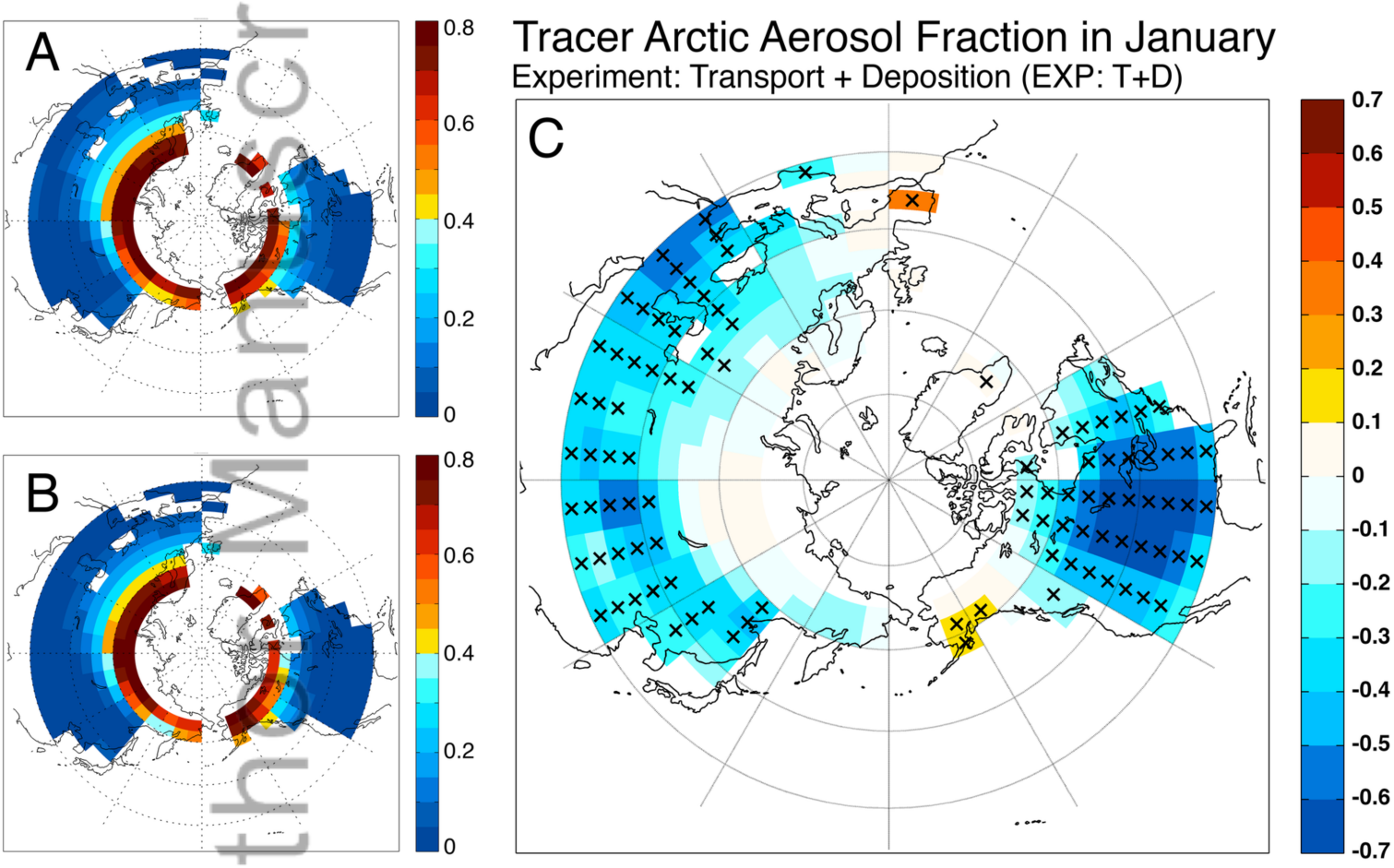

2015JD023964-f07-z-.png

(a) Relative Change of First Order Removal Rate (Annual Mean)

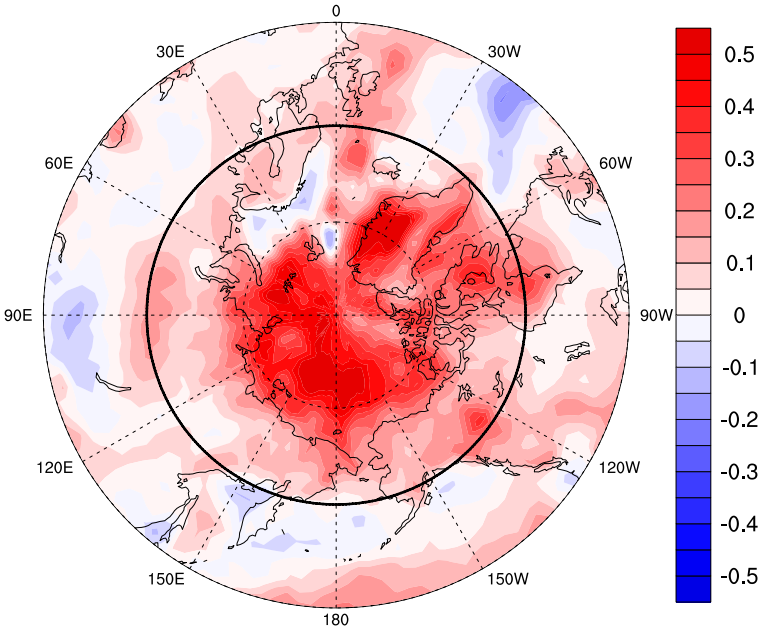

(b) Relative Change of First Order Removal Rate (January)

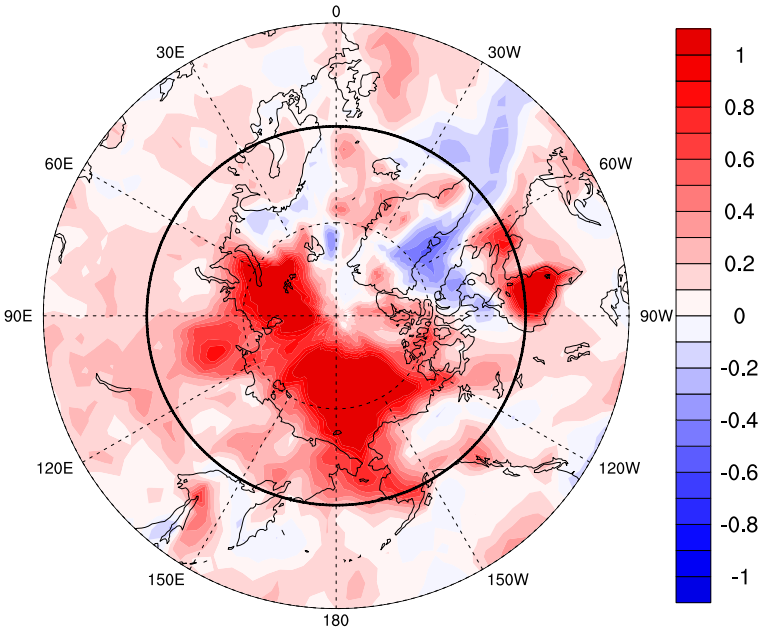

(c) Relative Change of First Order Removal Rate (July)

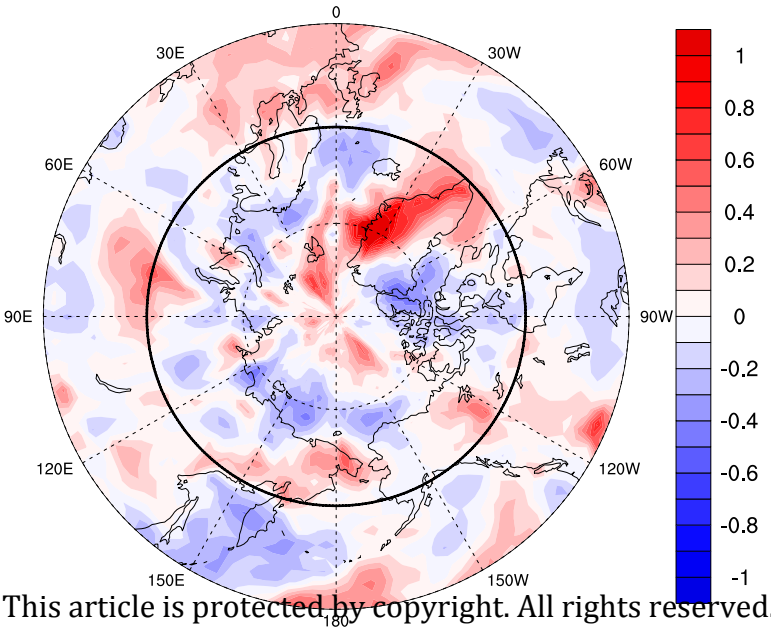

(a) Relative Change of Precipitation (Annual Mean)

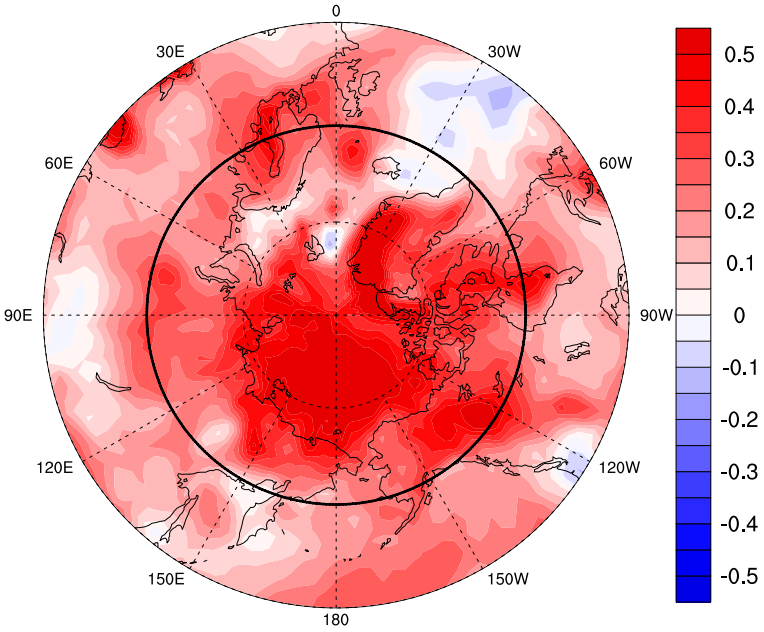

(b) Relative Change of Precipitation (January)

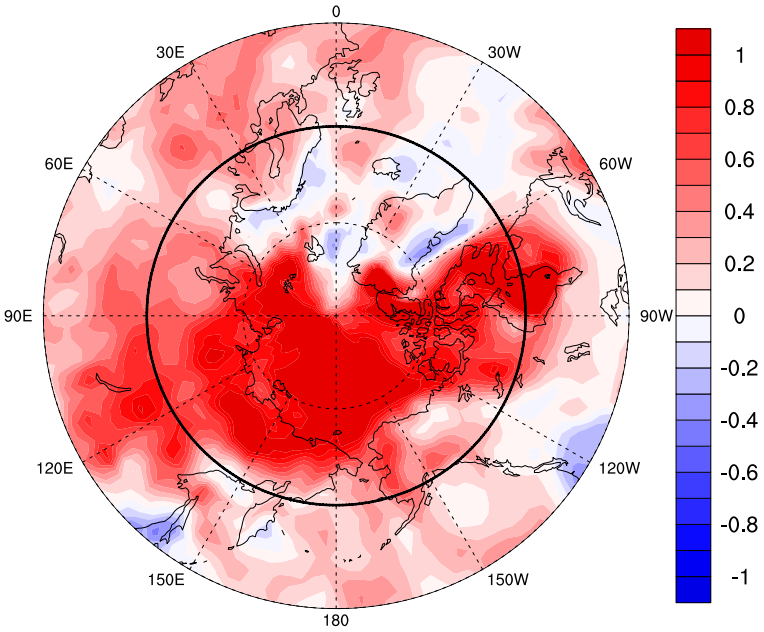

(c) Relative Change of Precipitation (July)

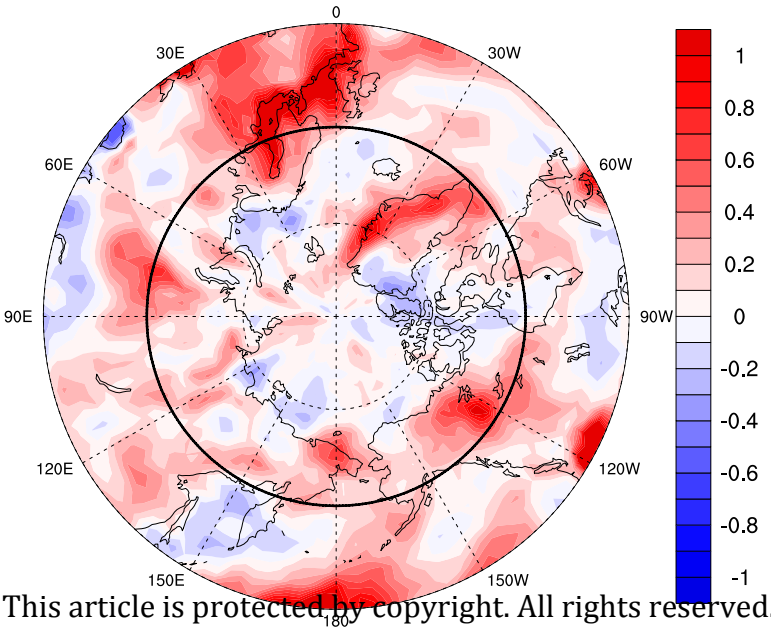

(a) Relative Change of BC Column Burden with (EpCf-EpCp)/EpCp

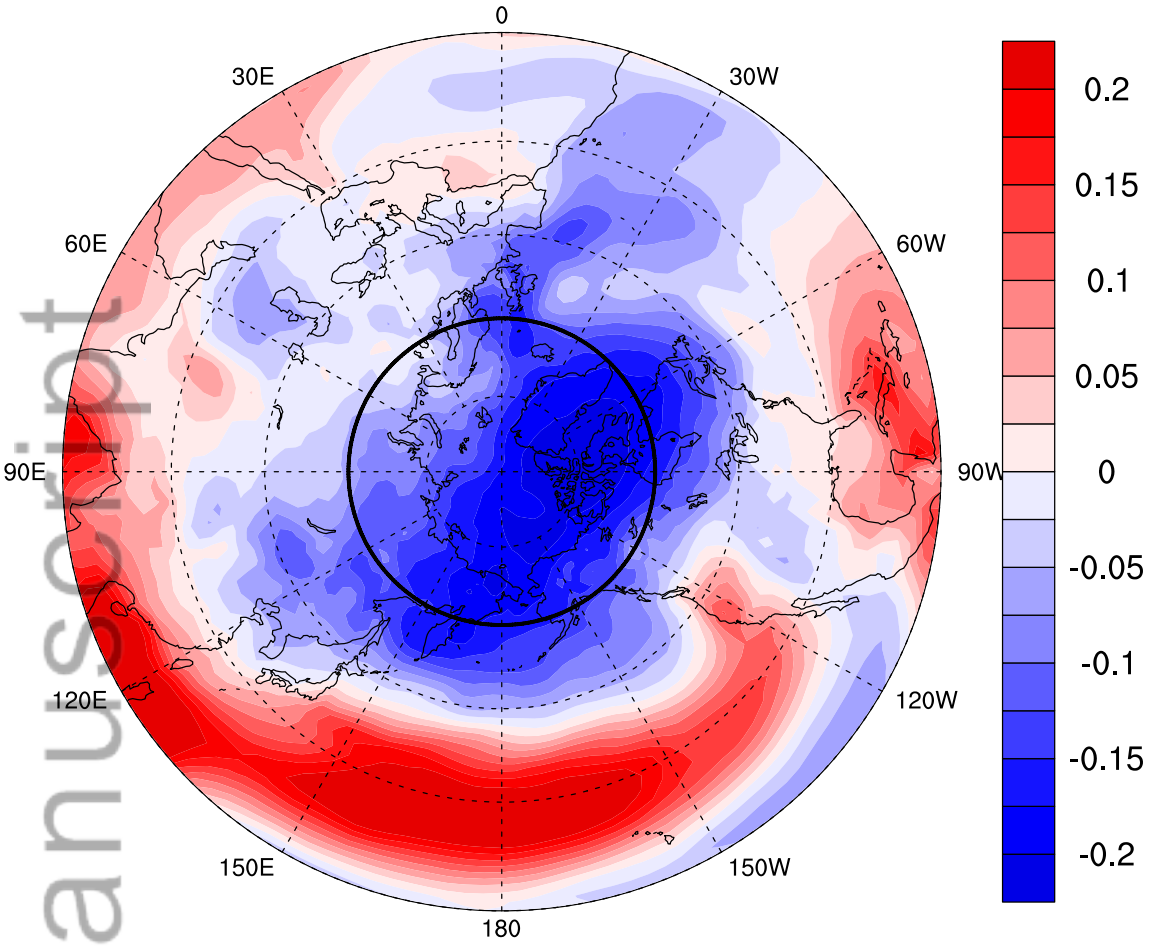

(b) Relative Change of BC Column Burden with (EfCf-EpCp)/EpCp